



Study on the relationship between urban land sprawl extension and urban thermal environment—taking Wuhan city as an example

Xuesong Li¹ · Baofeng Li² · Hong Chen²

Received: 28 November 2016 / Accepted: 1 October 2018 / Published online: 12 October 2018
© Springer-Verlag GmbH Austria, part of Springer Nature 2018

Abstract

In the twenty-first century, Wuhan has become one of the most rapidly developing cities in the world, accompanied by the changes of urban climate and environment. In order to explore the relationship between land extension and urban thermal environment in a quantitative way, the expansion of construction land in the southeast of Wuhan city was simulated using mesoscale weather forecasting model (WRF) of urban canopy model (UCM), based on Wuhan's geographical information, climate characteristics, urban function layout, regional development planning goals, and the equivalent of artificial energy consumption indicators. By summarizing and processing the calculated data, a series of meteorological values at key time points and during time periods were derived. Through quantitative analysis and comparison, conclusions about the effect of land spread in southeast of the city on urban microclimate in summer were obtained, which provides the theoretical basis for making the expansion strategy of construction land in Wuhan.

1 Overview

Due to the special historical background in the 1980s, cities in China have entered the stage of rapid development. As urban activities spread out to the suburbs and urban land area spreads out, the destruction of ecological environment and the change of thermal environment are resulted.

As a key city in central China, Wuhan is located in the east part of Jiangnan Plain and intersection of Yangtze River and Han River, and divided into three main districts, namely Wuchang, Hankou, and Hanyang. According to the State Council's approval on *Overall Urban Planning in Wuhan (2010–2020) in (2010)* No. 24 File (The State Council 2010), Wuhan will implement the unified urban and rural planning management, covering an area of 8494 km². Compared with the planning in 1999, Wuhan has grown by 5408 km², equivalent to a 2.75 times expansion. Regional superiority brings transportation strengths. Wuhan was selected as domestic first comprehensive transportation hub pilot

city in 2009, and in the next 5 years, the total investment on urban railway, aviation, and railway transportation projects is expected to reach 339 billion Yuan (Yangtze River Daily 2009). *2010–2020 Overall Urban Planning Overview of Wuhan* predicts that by 2020, Wuhan will have around 11.8 million permanent residents, including about 9.912 million urban population, and 5.02 million permanent residents in main urban areas, so more than half of people will live outside of main urban areas (Wuhan people's government 2010). Table 1 is population and geographic information of Wuhan in 2000, 2010, and 2020 (data in 2020 is the target value in planning overview) (Statistical Bureau of Wuhan 2001, 2011); Fig. 1 shows the status of Wuhan land (black grid is the current land and red grid is the new construction land in 2020). From the table and figure, it can be seen that the scale of urban planning in Wuhan will gradually spread and expand to the surrounding areas as time goes on. According to the research made by Dong and Cao (2016), from 1990 to 2010, the urban sprawl index of whole China was 2.417, that in the central region was 1.885 and that of Hubei Province was 2.641. This indicates that China's past urbanization strategies still focus on the expansion of urban space. Researchers analyzed China's cities using Zipf Law and concluded that current urban scale distribution system of China is still small; insisting on developing big cities is an inevitable trend. On this basis, Wuhan, the provincial capital in Central China, will inevitably continue its land extension and sprawl.

✉ Hong Chen
chhwh@hust.edu.cn

¹ School of Civil Engineering, Hubei University of Technology, Wuhan, China

² School of Architecture & Urban Planning, Huazhong University of Science and Technology, Wuhan, China

Table. 1 Population and geographic information of Wuhan city at 2000, 2010, and 2020

Location: 113°41'–115°05' East, 29°58'–31°22' North

	Total land area (km ²)	Built-up area (km ²)	Urban construction area in main urban areas (km ²)	Road length (km)	Total registered population (million)	Population in main urban areas (million)	Urbanization rate (%)
2000	8494.41	210	281.20	1332	7.4919	3.90	58.8
2010	8494.41	500	390	2800	8.3673	4.82	75
2020	8494.41		450	10,000	11.80	5.02	84

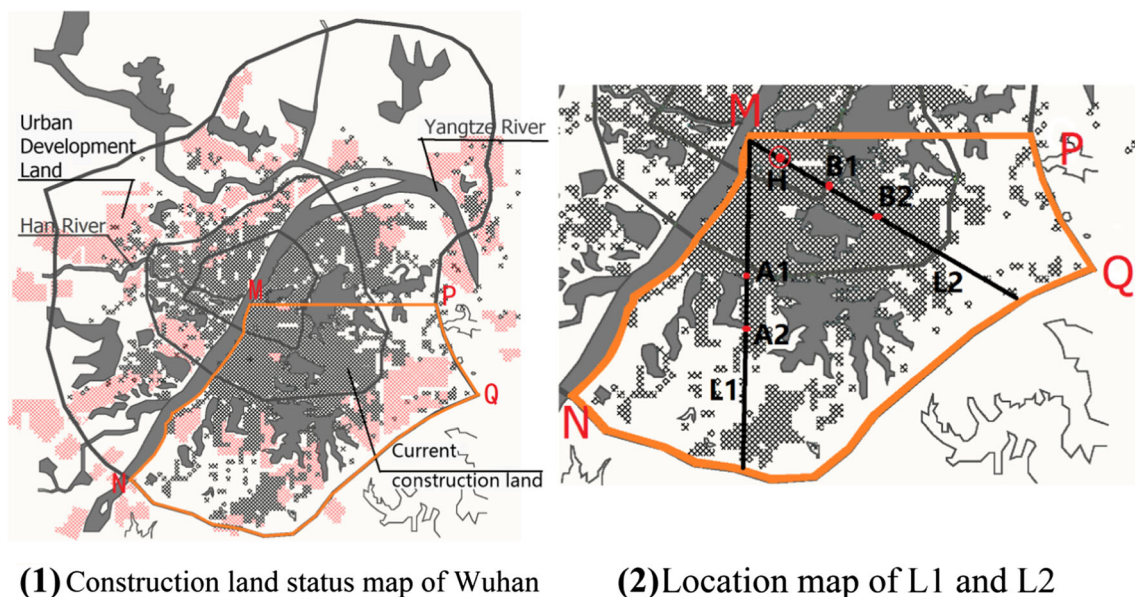
Note: The data in the table is derived from the statistical yearbook of Wuhan in 2000 and 2010, general urban planning outline for Wuhan from 2010 to 2020

Many scientists have been engaging in researches on urban climatic environment. *An Urban Approach to Climate-Sensitive Design: Strategies for the Tropics* written by M. Rohinton Emmanuel (2005) discusses the strategies and methods of urban design with climate adaptation from theoretical and practical aspects. *Climate Changes and Low-Carbon Urban Planning* written by Gu (2009) expounded the relationship between climate changes and urban planning as well as solutions and measures for China to cope with climate changes. In the late 1970s, Rao (1972) for the first time used thermal infrared remote sensing to study urban heat island. Halstead (1979) simulated the urban microclimate by computer; in 2000, Massachusetts Institute of Technology adopted CFD technology to simulate indoor and outdoor wind environment (Chen and Srebric 2000); Dr. Chen et al. (2009) from University of Tokyo employed the computer simulation method to study the thermal environment of two regions with different densities; Dr. Zhou et al. (2014) from Huazhong University of Science and Technology utilized WRF simulation technology to explore the impact of inland lake area change on urban climate; Pan and Li (2012) carried out

a research about the impacts of underlying surface changes on climate precision by WRF in Heihe River basin region; Li et al. 2014 carried out WRF simulation to study the impact of increased urban plot ratio on urban thermal environment. This paper will discuss impacts of urban land sprawl extension on urban climate by the couple technology of UCM (urban canopy model) and WRF (weather research and forecasting).

2 Relationship between the property of underlying surface and urban thermal environment

The development of urban construction land can be divided into two modes. The first refers to the increase of intensity of construction land, that is, the high-density development of urban construction land. The second refers to spreading of urban construction land to the suburbs, so that the natural underlying surface of fringe areas changes into artificial underlying surface. Both developing modes lead to changes in the urban thermal environment. In physics, the moment of inertia refers to the scale

**Fig. 1** Present construction land status map of Wuhan. Note: the black grid is the current land and the red grid is the new construction land in 2020

by which a substance prevents its temperature from changing, and the specific heat capacity refers to the heat storage capacity of a substance. The artificial earth surface consisting of sand, concrete, and asphalt has larger thermal inertia and specific heat capacity than the natural earth surface. Especially in the summer daytime, abundant sunshine makes the artificial surface absorb more heat, but it does not enjoy good evaporation and transpiration function like the natural surface (Gao et al. 2001). During the day, urban artificial underlying materials continue to absorb heat. At night, when the local surface releases heat into the sky by means of convection, conduction, and long wave radiation, the buildings also impede the heat release inside the urban canopy. As a result, the time for urban underlying surface to reach low temperature equilibrium is extended, and the urban heat island effect is strengthened.

There are two main factors causing the change of airflow in the near-earth atmosphere, one is the roughness of the underlying surface and the other is heat. The rough structure of the city's surface and the increased release of man-made heat enhance the thermodynamic activity of the air in the near-earth atmosphere. Therefore, there is an impact on the airflow passing over the city, causing the change of airflow velocity and direction, forming stable airflow area, positive pressure area, aerodynamic wind shadow area, and wake flow area (Xu 2003). Vortices and turbulence of various directions are formed between urban buildings and open spaces. These vortices and cyclones can blow up dust, bacteria, and various particulate pollutants from the city's surface, letting them float in the air. This not only pollutes the urban environment, but also reduces the power of the airflow passing over the city, which reduces the wind speed, slows down the heat dissipation, and also leads to the enhancement of the heat island effect.

3 Weather research and forecasting on urban canopy model

3.1 Research method

In this paper, the thermal environment of Wuhan was investigated using the mesoscale weather research and forecasting (WRF) based on urban canopy model (UCM). WRF (weather research and forecasting) is a new mesoscale forecasting pattern and assimilation system developed by American meteorological field. The current common version also couples single-layer (UCM) into (WRF) pattern (Zhang 2004). The effect of underlying surfaces with different attributes on atmosphere can be reflected by adjusting the parameters of the underlying surface in urban areas, such as reflectivity and roughness. WRF considers factors such as geometric features of urban canopy, shielding of buildings against radiation, and the reflection of buildings on short and long waves. The basic characteristics of the model include physical characteristics of boundary layer

(Mellor and Yamada 1982), physical characteristics of surface layer (Monin and Obukhov 1954), physical characteristics of surface (Ek et al. 2003), procedure of micro-physics (Thompson et al. 2004), radiation characteristics of short and long waves (Mlawer et al. 1997; Mielikainen et al. 2012), and application of Noah land surface model (LSM) (Chen and Dudhia 2001). The mathematical model is shown below:

$$C(\theta) \frac{\partial T}{\partial t} = \frac{\partial}{\partial z} \left[K_t(\theta) \frac{\partial T}{\partial z} \right] \quad (1)$$

In the ground heat flow equation, T , C , K_t , and θ represent the soil temperature (K), heat capacity per unit volume ($\text{Jm}^{-3}\text{K}^{-1}$), and thermal conductivity ($\text{Wm}^{-1}\text{K}^{-1}$), respectively. They are represented by Eqs. (2), (3), and (4).

$$C = \theta C_{\text{water}} + (1 - \theta_s) C_{\text{soil}} + (\theta_s - \theta) C_{\text{air}} \quad (2)$$

The heat capacity per unit volume is $C_{\text{water}} = 4.2 \times 10^6 \text{Jm}^{-3}\text{K}^{-1}$, $C_{\text{soil}} = 1.26 \times 10^6 \text{Jm}^{-3}\text{K}^{-1}$, and $C_{\text{air}} = 1004 \text{Jm}^{-3}\text{K}^{-1}$ with peak soil humidity.

$$K_t(\theta) = \begin{cases} 420 \exp[-(2.7 + P_f)], & P_f \leq 5.1 \\ 0.1744 & P_f > 5.1 \end{cases} \quad (3)$$

$$P_f = \log \left[\Psi_s(\theta_s/\theta)^b \right] \quad (4)$$

Here Ψ_s and b are saturated soil potential and curve-fitting parameter based on the soil type.

$$\frac{\partial \theta}{\partial t} = \frac{\partial}{\partial z} \left(D \frac{\partial \theta}{\partial z} \right) + \frac{\partial K}{\partial z} + F_\theta \quad (5)$$

Equation (5) is the prediction of hydrological model, in which D and K are respectively the diffusivity and hydraulic conductivity of soil water, and both of them are function of θ ; F_θ represents the source and sink, i.e., rainfall, evaporation, and runoff volume of soil.

D , $K(\theta)$, and $\Psi(\theta)$ can be expressed by Eqs. (6), (7), and (8) respectively, as below.

$$D = K(\theta) \frac{\partial \Psi}{\partial \theta} \quad (6)$$

$$K(\theta) = K_s(\theta/\theta_s)^{2b+3} \quad (7)$$

$$\Psi(\theta) = \Psi_s / \left(\frac{\theta}{\theta_s} \right)^b \quad (8)$$

K_s is the saturated hydraulic conductivity of soil.

$$E = E_{\text{dir}} + E_c + E_t \quad (9)$$

Equation (9) shows the evaporation model of water, where E is total evaporation, E_{dir} is direct evaporation, E_c is intercepted evaporation by plants, and E_t is evaporation volume from leaves and roots. All parameters are defined in Eq.

(10)–(14). E_p is potential evaporation, σ_f represents the part covered by green plants, θ_{ref} represents the capillary water content in soil, θ_w represents wilting point, W_c represents intercepted canopy water content, S denotes the maximum canopy capacity, D denotes the excess precipitation or drip, P denotes input total precipitation, and B_c denotes the function of canopy resistance and $n = 0.5$.

$$E_{dir} = (1 - \sigma_f) \beta E_p \quad (10)$$

$$\beta = \frac{\theta_l - \theta_w}{\theta_{ref} - \theta_w} \quad (11)$$

$$E_c = \sigma_f E_p \left(\frac{W_c}{S} \right)^n \quad (12)$$

$$\frac{\partial W_c}{\partial t} = \sigma_f P - D - E_c \quad (13)$$

$$E_t = \sigma_f E_p B_c \left[1 - \left(\frac{W_c}{S} \right)^n \right] \quad (14)$$

3.2 Parameter settings and simulation verification

To fully reflect the impact of the change in urban underlying surface properties on urban climate, the calculation region and position were set, and grid description of calculation region is shown in Table 2. All land within the outer-ring road of Wuhan are included in Domain3 (see Fig. 3), where the central point is at 114.30° E, 30.50° N. Horizontal grid resolutions of Domain3, Domain2, and Domain1 are 0.5 km, 1.5 km, and 4.5 km, respectively. Domain1 provides boundary condition for Domain2, while Domain2 provides boundary condition for Domain3. In the model, the segment from the ground up to 20-km height is divided into 35 layers in vertical direction. The original data of Wuhan land use was collected from the database on land use and land cover in United States Geological Survey (USGS), and then modified based on the actual situation in Wuhan. According to USGS-24 global land use information data (National Center of Atmospheric Research 2012), there are totally eight categories of land use in Wuhan: urban, dry land crop (Dryland C.P.), irrigation crop (Irrig. C.P.), crop/grass mosaic (C/G. Mosaic), crop/wood mosaic (C/W. Mosaic), grassland, shrub land, and water.

Scholars have constantly improved WRF + UCM pattern and made verification tests for several times (Dudhia 1993; Keyser

and Anthes 1997; Cleugh and Oke 1986). In 2001, Kusaka et al. (2001) compared the results measured in Vancouver, British Columbia and the results measured in Nagahama of Japan and found that the two results agreed well with each other. Dr. Zhou Xuefan from Huazhong University of Science and Technology compared the air temperature value measured at a certain point in Wuhan city from August 13 to August 16, 2011, with the simulated air temperature at a 2-m height, and the two results were consistent with each other (Zhou et al. 2014). The reliability of method was verified in this study. The global meteorological data from National Center for Atmospheric Research (NCAR) NECP/NCAR fnl was adopted as the boundary conditions. For the roof surface, wall surface, and road surface, their heat capacities were set to $1.0E6 \text{ J m}^{-3} \text{ K}^{-1}$, $1.0E6 \text{ J m}^{-3} \text{ K}^{-1}$, and $1.4E6 \text{ J m}^{-3} \text{ K}^{-1}$, respectively, the thermal conductivity values were respectively set to 0.67, 0.67, and $0.4004 \text{ J m}^{-1} \text{ K}^{-1} \text{ S}^{-1}$, the absorptivity was set to 0.90, 0.90, and 0.95, respectively, and the reflectivity was to 0.20. The intensity of land use and other parameters are shown in Table 4. The climatic data from August 12 to 16, 2011, are input as original values for simulation computing. We extracted a simulated temperature 2 m vertically above the ground at a certain road section in Xongchu Avenue, Wuhan at 21:30 pm on August 13, 2011, and compared it with the actual temperature on the same road section at the same moment (Li and Chen 2012), as shown in Fig. 2. It could be found out that they were quite close to each other. As a result, we believe that UCM + WRF simulation is an accurate and reliable method to study “the effect of the change in urban surface property on urban climate and thermal environment.”

4 Case settings

Located in the inland, Wuhan belongs to the alluvial plain with residual hilly rivers and lakes, in basin topography. Wuhan is rich in water and very hot in summer, which belongs to a northern subtropical humid monsoon climate. The temperature

Table 2 Computational domains and grid detail

	Domain size (X × Y × Z)	Grid number	Grid size (km)
Domain1	459 × 540 × 20	102 × 120 × 35	4.5
Domain2	153 × 180 × 20	102 × 120 × 35	1.5
Domain3	51 × 60 × 20	102 × 120 × 35	0.5

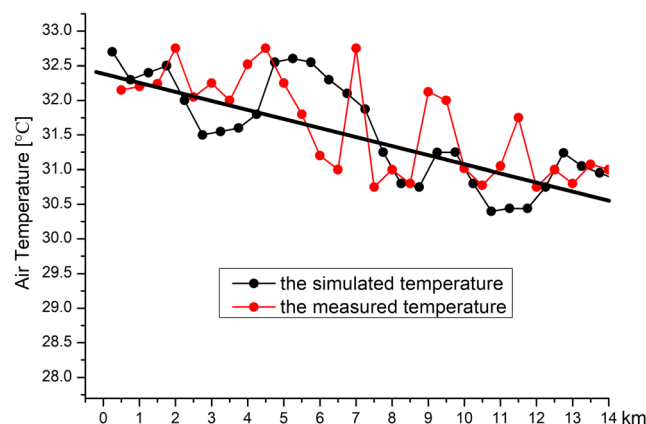


Fig. 2 Comparison of simulated temperature and measured temperature

in Wuhan in July and August can reach 37 to 39 °C, the summer lasts over 130 days, with the southeasterly wind as the dominant wind. Since the southeast of the city is a high-education and high-tech industrial concentration, this city has a high probability to expand to the southeast. Therefore, this paper selected MPQN in southeast Wuhan (see Figs. 1 and 3) to study the impact of construction land expansion on urban climate. According to variable requirement of parameter factors in WRF software as well as the interim provisions on the general urban planning of Wuhan and the intensity management of construction land in Wuhan's main urban area from 2006 to 2020, we divided Wuhan into three areas with different land use intensity (see Fig. 3). The first area is the main urban area, which is also known as the first circle (area with high land use intensity); the second circle (area with medium land use intensity); the third circle (area with low land use intensity). The case setting is shown in Table 3. The setting of land use intensity and other parameters is shown in Table 4. After comparing the meteorological data of many years, we selected the meteorological value with the characteristics of Wuhan hot summer climate in August 2011 for simulation.

5 Analysis on simulated results

After WRF + UCM calculation for Case1, Case2, and Case3, some meteorological values of Domain3 on August 13, 2011, were collected for comparison. These values can intuitively and quantitatively reflect urban climate change as the city expands in upwind direction. All meteorological values in this paper correspond to Beijing time.

5.1 Analysis and comparison of temperature fields and temperature difference fields of three cases

Figures 4, 5, and 6 show temperatures and wind fields of three cases in Domain3 at representative moments. At 5:00 am in

summer, the urban heat island area increases slightly with the expansion of the southeast part of the city, which is especially significant in the east part of the Yangtze River. The urban heat island phenomenon is very prominent at night for all cases. At 20:00 pm: Case3 has the largest expansion of urban construction land, and thus has larger urban heat island range and intensity than other cases. At this time for Case2, the heat island range is relatively small, and then the heat island intensity begins to weaken (see Figs. 5, 13).

In order to further analyze the differences in temperature and wind field among the cases and related causes, we extracted the temperature difference field and wind field at 5:00 and 14:00, as shown in Fig. 6(Case2-Case1, Case3-Case1). As can be seen from Fig. 6, during these two periods of time, the expansion of construction land has no significant impact on urban temperature. However, it is worth noting that the blue circle in (Case3-Case1) shows obvious negative and positive temperature difference patches. These patches are water in Case1 and Case2 and become construction land in Case3. Construction land is composed of sand, concrete, asphalt, and other materials. Its specific heat capacity and thermal inertia are smaller than water body, but the absorption and release rates of thermal energy are faster. Therefore, after a night of cooling, more heat is lost from the construction site, and temperatures near the surface are lower in the early morning (Fig. 6(2)). However, the transpiration of construction land is weaker than water body, so the temperature near the surface of construction land is higher than that of water body (Fig. 6(4)). At 14:00, positive temperature patches appear in the green circle (Fig. 6(3, 4)). This is the result of local temperature rise caused by the change of surrounding wind environment due to the expansion of urban underlying surface.

At night, the larger the expansion of the construction land is, the larger the range of positive temperature difference is, the higher the intensity is (Fig. 7). In Case2, there is no buried water area when construction land is expanded, and a ventilation corridor is set through from south to north (1-Tangxun Lake,

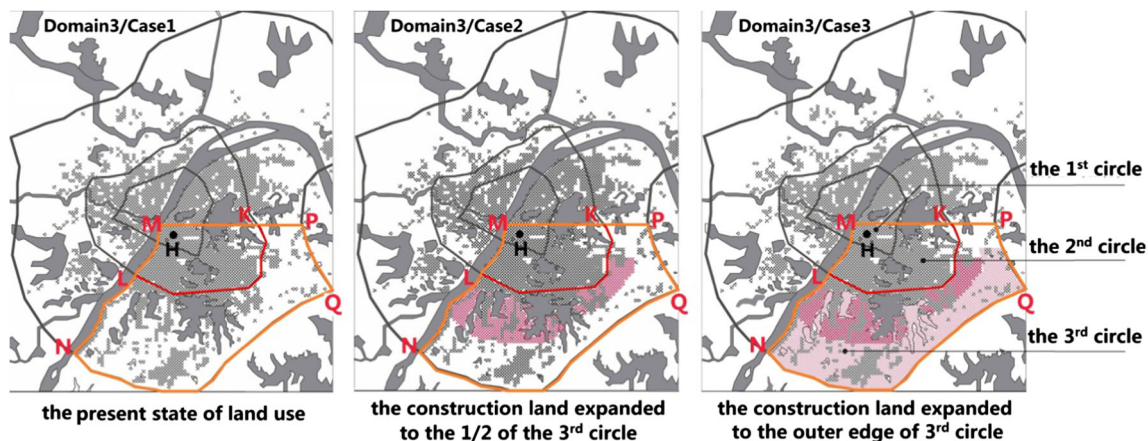


Fig. 3 Land extension scheme in southeast Wuhan

Table 3 Case settings

	Case1	Case2	Case3
Case description	Present construction land	Urban construction land expanded to the 1/2 ring of third land use intensity area	Urban construction land expanded to outer edges of third land use intensity area

2-South Lake, 3-East Lake, 4-Yangtze River, and 5-Wu Lake). At 20:00, the expansion of construction land increases temperature and air thermal power, while the roughness in the corridor is lower than that on both sides of the corridor. Therefore, more airflow is from south to north through the corridor, taking the heat away by the way, and wind speed V_{Case2} is gradually greater than V_{Case1} from south to north, and urban wind system changes. As shown in Fig. 7(1), Case2-Case1 show a significant negative temperature difference. In Case3, part of the water surface of Tangxun Lake has been changed into construction land, where the positive temperature difference is obviously strengthened. In Case3, in addition to the increase of the heat release of man-made heat, the surface roughness is increased as the passage of air flow is blocked, so the wind environment inside the city is not improved, the characteristics of low wind speed are more significant, and the range of urban heat island is expanded significantly (Fig. 7(2)). At 24:00, the positive temperature difference field has spread from south to north to the northern part of the city (downwind area) with prevailing winds in (Case2-Case1), while in Case3, as construction land expands, natural ventilation corridors are blocked and air mobility is reduced. The southeastern part of the city (upper wind region) of (Case3-Case1) still has obvious positive temperature difference (see Fig. 13).

5.2 Analysis and comparison of wind fields of three cases

Expanding urban construction lands will change the properties of underlying surface and roughness of earth surface as well as increase the artificial heat release. Figure 8 shows the wind field (wind direction and wind velocity) at 10-m height within the range of Domain3 at 4 typical time periods for 3 cases. At

5:00 am, the temperature is at a low point, with low heat and kinetic energy, and the wind speed in each case is also very low, varying between 2 and 3 m/s. The difference in urban wind direction among cases shows at the downwind area. As shown in Fig. 8(1), at 14:00, the temperature reaches the maximum, the heat and kinetic energy are the largest of a day, and the wind speed in the city reaches the maximum. At this time, the wind direction along the Yangtze River and the coast is basically parallel to the river course. In the northwest of the city (Hankou area), the difference in wind direction is the most obvious, followed by that in the southeast of the city (Wuchang area), and that in the southwest (Hanyang area), as shown in Fig. 8(2). At 20:00, due to the special topographic features of “three banks and two rivers” of Wuhan city, the wind speed shows a gradual weakening from the east and south suburbs to the northwest. In particular, the wind speed of Hankou as the center of the city is the smallest, and the wind direction in the city gradually shifts from southeast to south and west, showing a special heat island circulation phenomenon, as shown in Fig. 8(3). At this time, all cases show significant difference in wind direction at the region where the wind speed is higher. At 24:00, as the cooler air from suburban upwind gradually seep in, the heat has gradually shifted from the site where surface attribute changes to the downwind of the city, the heat energy and kinetic energy decrease in the southeast of the city, and the wind speed is the minimum. However, the wind speed in the north, northeast, and southwest of the city is greater than that in the southeast of the city. According to the wind field figure from 20:00 to 24:00, the urban ventilation corridor composed of five lakes in Case2 makes the wind speed in the central area of the city significantly higher than that in the other two cases. The simulation results also show that the change of wind direction in the

Table 4 Land use intensity and other parameters

	The first land use intensity area (33)	The second land use intensity area (32)	The third land use intensity area (31)
Roof level [m]	30	21	18
Roof width [m]	55	30	30
Greening rate [%]	30	30	30
Frc_urb [fraction]	0.7	0.7	0.7
Road width [m]	20	20	20
Anthropogenic heat [W/m^2]	90	60	40

Note: parameters are based on detailed geographic information; 31, 32, and 33 are the three default modifiable urban types of land use in the mode (WRF + UCM)

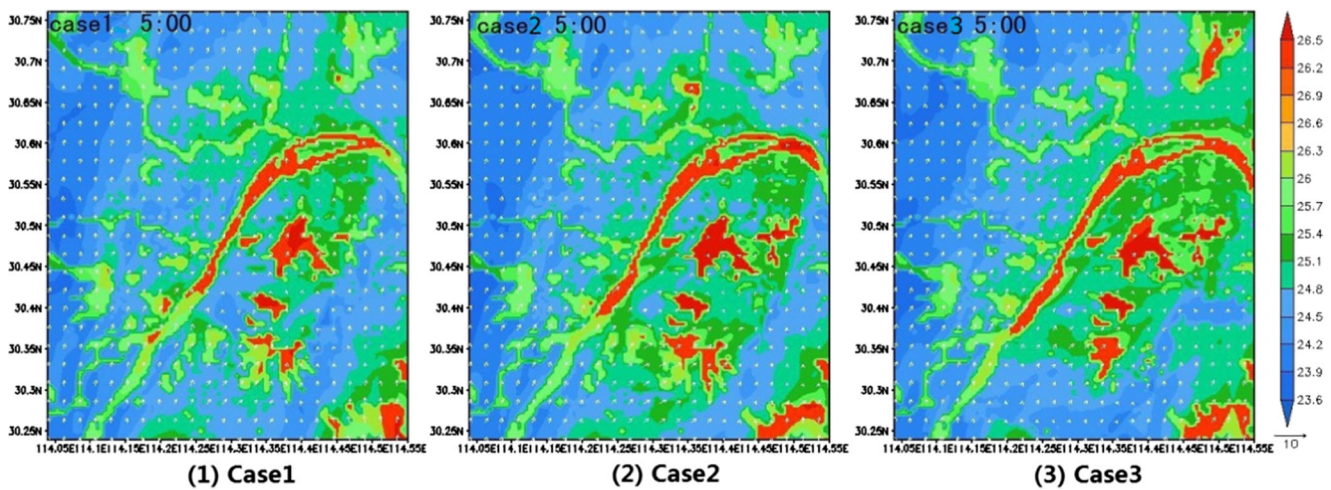


Fig. 4 Temperature and wind field at 5:00 for Case1, Case2, and Case3

southeast of the city is more significant than the change of wind speed.

5.3 Comparison of full-day average temperature and energy curves of cases in southeast Wuhan

The impact on regional urban temperature field by construction land extension in southwest Wuhan has been analyzed in previous sections. Then, we analyzed all-day temperature weighted average in MPQN area (Southeast of the city) and KPQNL area (Surface attribute variation) for three cases, as shown in Fig. 9. From 0:00 to 5:00, it can be seen that the temperature follows $T_{\text{Case3}} > T_{\text{Case2}} > T_{\text{Case1}}$ can be seen. This indicates that with the expanding of construction land, the average temperature gradually increases during this period. These three curves all approach to 25 °C as time goes on and reach its minimum at 5:00–6:00. Underlying surface starts to obtain solar radiation energy from 5:48 when the sun rises. From 6:00 to 12:00, solar radiation has a key effect on urban temperature: average temperature curves of three cases in the

two regions coincide (MPQN\KPQNL), while land expansion has less influence on the urban temperature. Earth surface accumulates massive heat after morning-long solar radiation. Since the artificial earth surface has no transpiration and evapotranspiration function as natural surface does, the larger the area of urban construction land is, the more heat accumulates, the greater the heat radiates into the air, and the higher the air temperature is inside the urban canopy. Therefore, T_{Case3} reaches maximum, T_{Case1} reaches minimum, and T_{Case2} lies between T_{Case3} and T_{Case1} during 12:00–24:00. We can see from Fig. 9 that the temperature in the urban canopy reaches maximum during 15:00–17:00, after which the temperatures of three cases start to drop obviously as the solar radiation weakens, and finally tends to be stable until 22:00. Average temperature curves of Case1 and Case2 in MPQN almost coincide from 5:00 to 20:00, and then start to separate from each other: $T_{\text{Case2}} > T_{\text{Case1}}$; T_{Case1} and T_{Case2} in KPQNL start to separate from each other at 19:00, and $T_{\text{Case2}} > T_{\text{Case1}}$, which is at least an hour earlier than the separation in MPQN. This indicates that more heat is produced by property

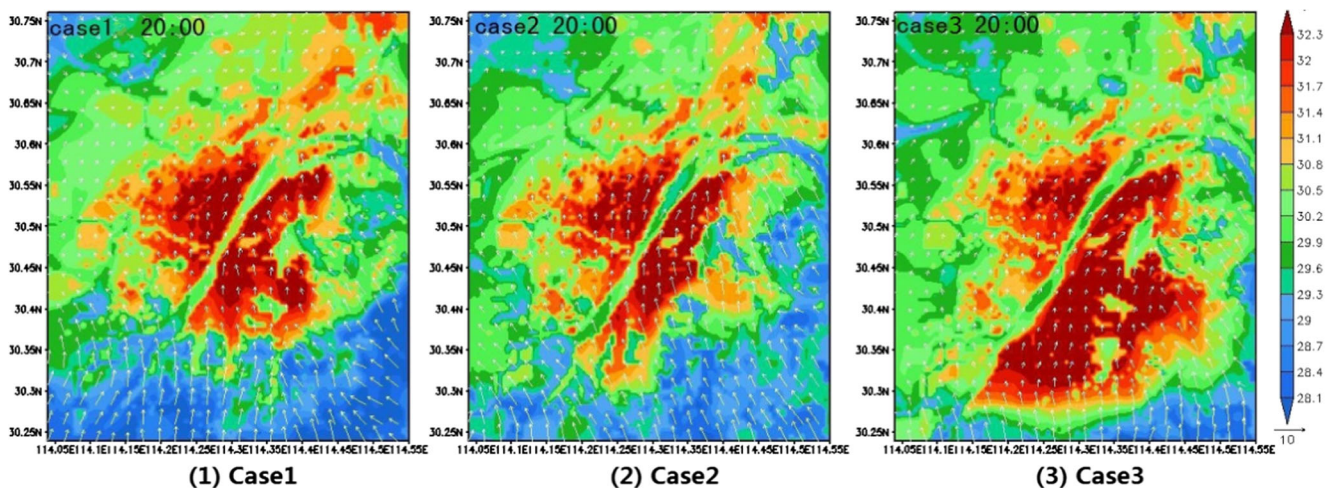
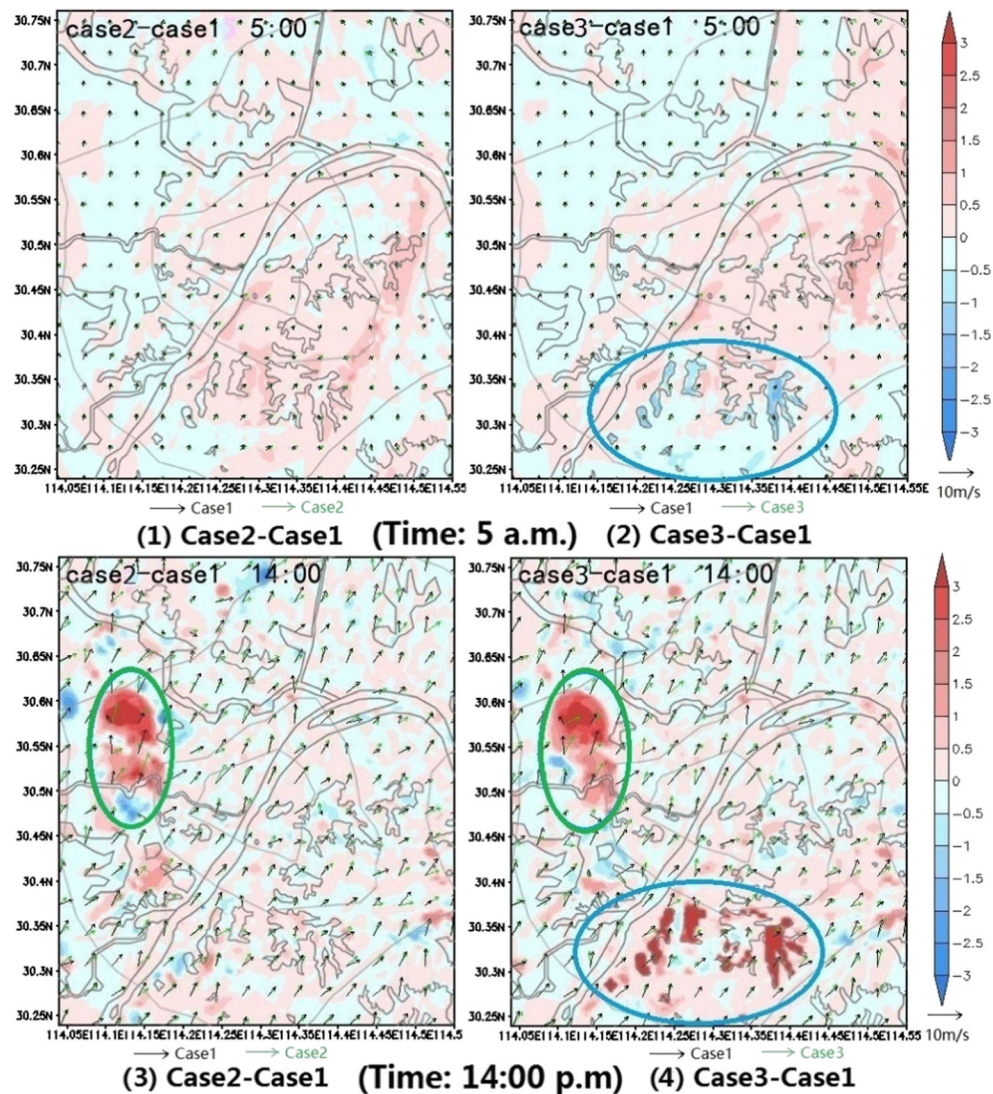


Fig. 5 Temperature and wind field at 20:00 for Case1, Case2, and Case3

Fig. 6 Temperature difference and wind field at 5:00 and 14:00 for Case2-Case1, Case3-Case1



change of underlying surface in Case2 than in Case1, and exceeding heat will first increase the temperature in its region, and then carried by the wind to downwind regions to cause a wide range of temperature increases 1 h later. The local sunset time is 19:07, after which urban underlying surface mainly releases heat into air. In Case3, the construction land area expands greatly, and heat dissipation increases. However, the heat inertia of the retained water in Case2 is large, so the heat dissipation time is longer than that in Case3, thus resulting in $T_{\text{Case2}} = T_{\text{Case3}} > T_{\text{Case1}}$ during 22:00–23:00. Although there are water bodies in Case1, the surrounding areas are all natural surface, and the average temperature in the two areas (MPNQKPQNL) is the lowest.

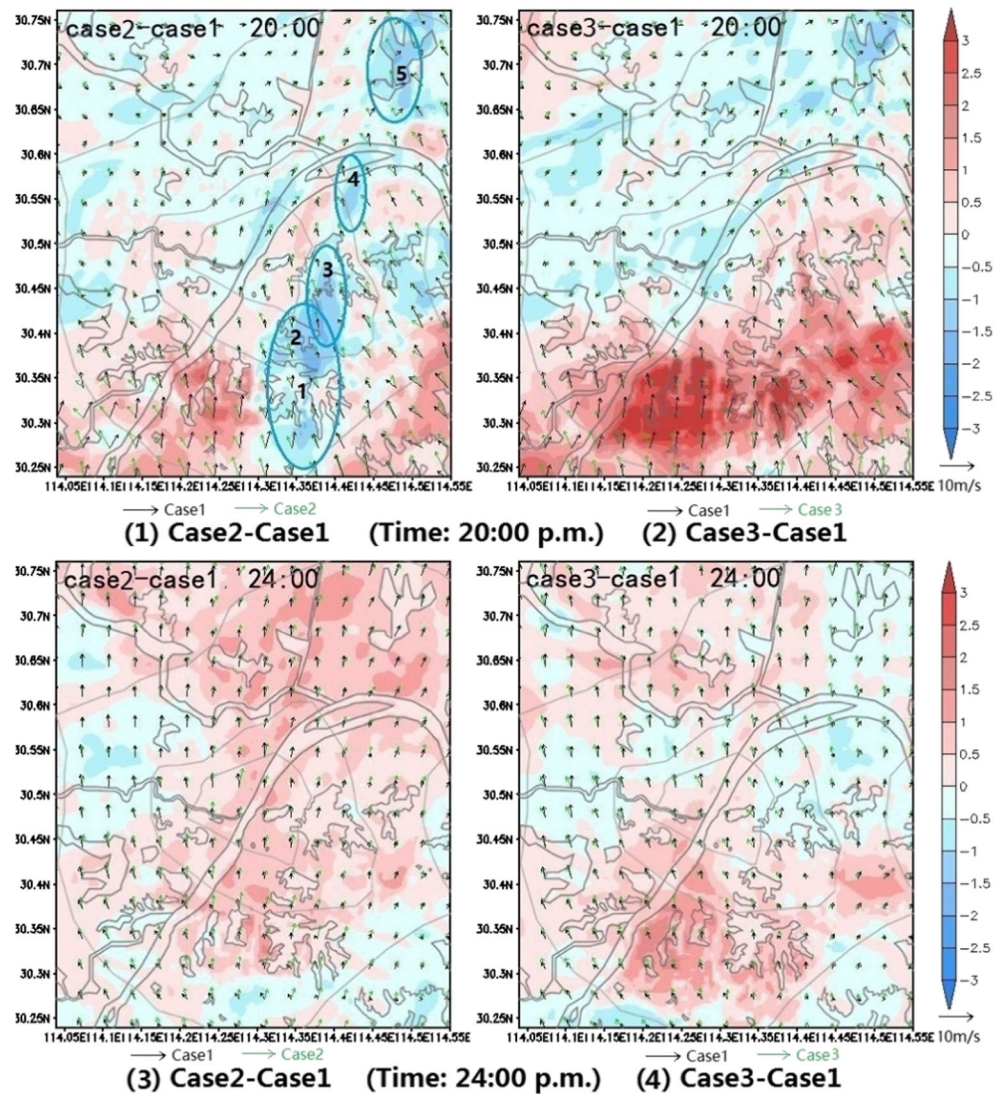
Here below are parts of energy values of three cases in KPQNL block (see Fig. 10):

Rn: “DOWNWARD SHORT WAVE FLUX AT GROUND SURFACE”, The values of all cases are basically the same.

H: “UPWARD HEAT FLUX AT THE SURFACE”; As the construction land proportion gradually increases, $H_{\text{Case2}} > H_{\text{Case1}}$, so the temperature increases;
 LE: “LATENT HEAT FLUX AT THE SURFACE”; As the construction land proportion gradually increases, LE gradually decreases: $LE_{\text{Case1}} > LE_{\text{Case2}} > LE_{\text{Case3}}$, which is the most significantly from 6:00 to 18:00;
 G: “GROUND HEAT FLUX”; As the expanding of construction land, G value shows an increasing trend: $|G_{\text{Case3}}| > |G_{\text{Case2}}| > |G_{\text{Case1}}|$.

The energy curve shows that, under identical shortwave radiation, the heat flux value of ground surface increases after the natural underlying surface is transformed into artificial underlying surface. In particular, after part of the water in Case3 is converted into construction land, the moisture heat exchange between the surface and the atmosphere decreases, that is, partial latent heat flux is transformed into sensible heat flux, and

Fig. 7 Temperature difference and wind field at 20:00 and 24:00 for Case2-Case1, Case3-Case1



the air temperature in the city naturally increases. Therefore, it can be concluded that the expansion of urban construction land and the change of underlying surface property can directly affect the change of urban thermal environment.

5.4 Comparison on temperatures of cases on axis L1\L2

Figure 11 shows the location of two different directional axes L1 and L2 in the southeast of the city, originating from M point. In order to display the temperature change from the central zone to the edge zone in a more intuitive way, we extracted the 2-m-high temperature value on the axes L1 and L2 for research. As the A1-A2 section in axis L1 and B-1B2 section in axis L2 are adjacent to the water surface, but the distances between their locations and the water surface are different, so they will not be discussed in this study. According to the results of our mobile test, in the summer

night, the Yangtze River in Wuhan has a certain cooling effect on the temperature of air within about 2.0 km along its coast (Li and Chen 2012), but the situation is complex, which will not be discussed in this study as well. In order to reflect the status of urban heat island, temperature values on the two axes at 20:00 and 24:00 were analyzed. From Figs. 12 and 13, we can see that the temperature on the axis L1\L2 gradually decreases from the urban center to the edge zone, showing significant urban heat island phenomenon.

At 20:00, the phenomenon of heat island circulation is significant. Due to the different degree in expansion of the construction land, different artificial energy dissipation, and different daytime surface heat storage increment, as well as the change in roughness of the underlying surface; the urban heat island circulation in each case is different. In Case1 and Case2, no water is replaced at the southeast margin, and the differences of wind environment in the main urban area are not significant. However, part of water in Case3 is replaced by

Fig. 8 Comparison of wind field of Case1, Case2, and Case3 at typical time

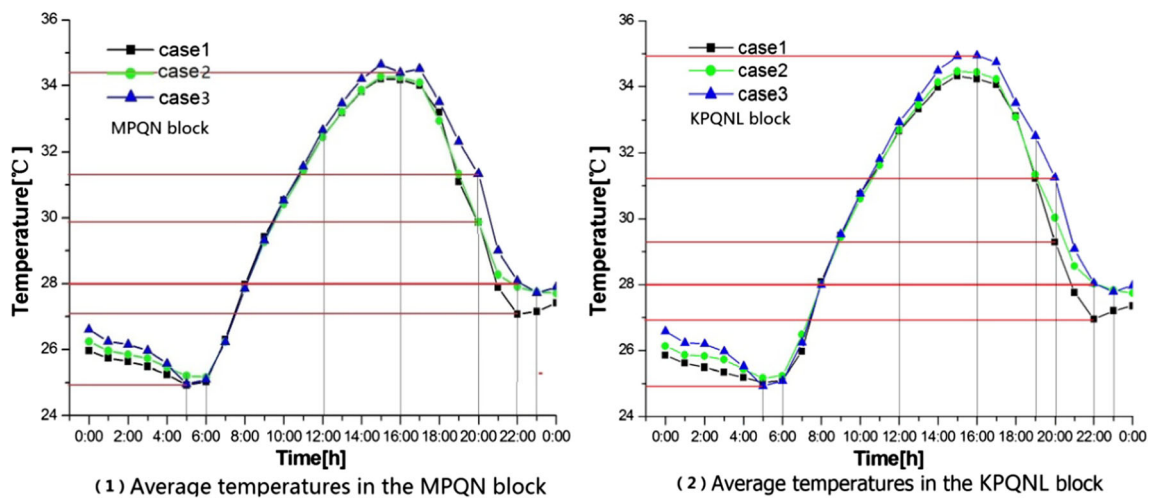
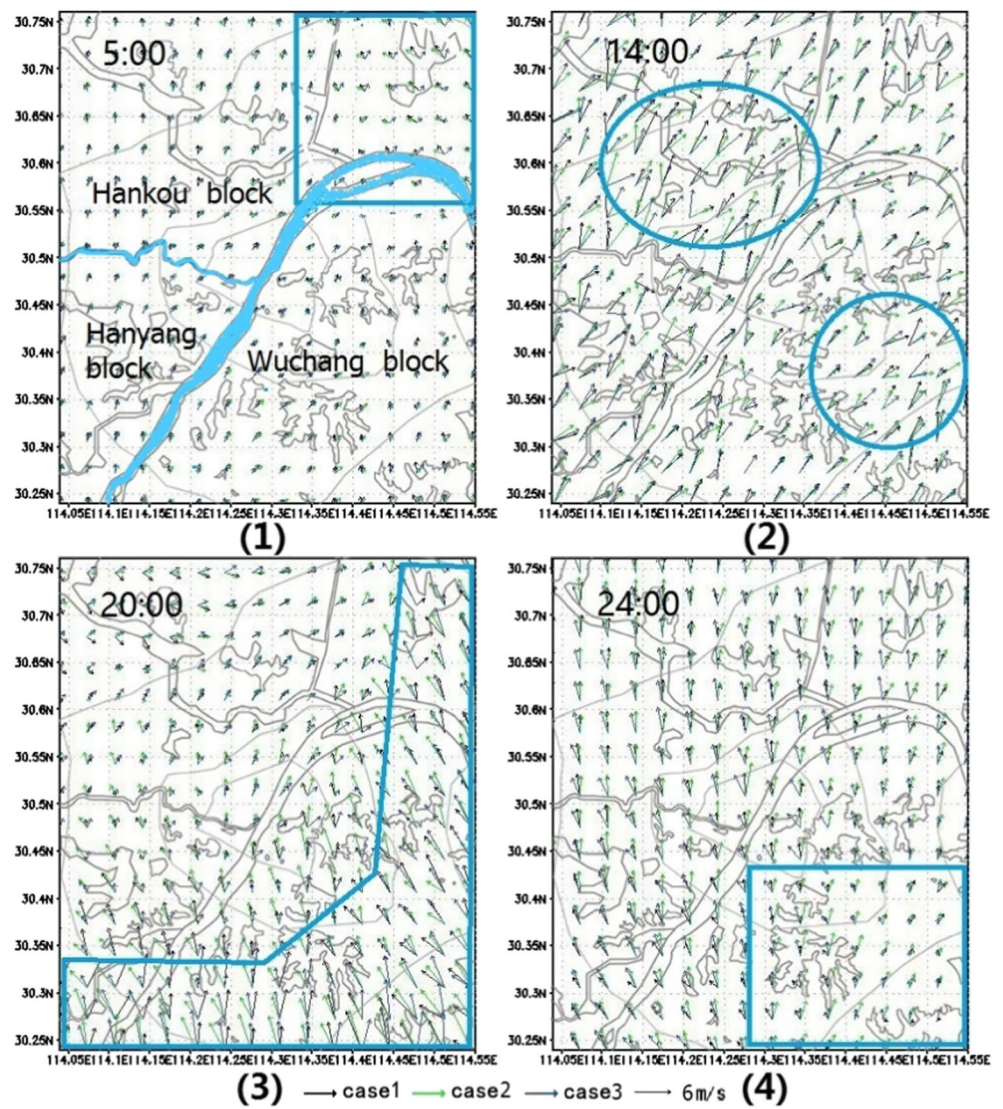


Fig. 9 Full-day average temperatures of Case1, Case2, and Case3 in MPQN/KPQNL block

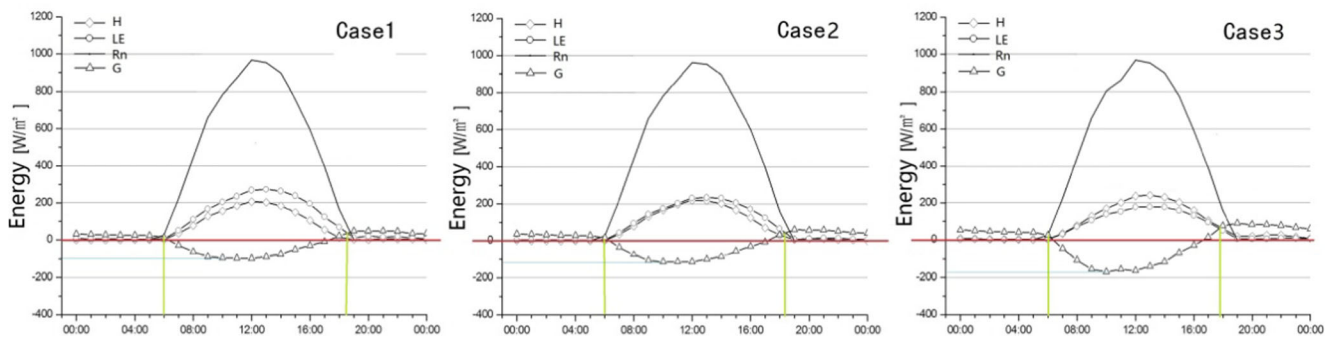


Fig. 10 Energy curves of Case1, Case2, and Case3 in LNQPK block

construction land, the air inlet of the air duct is blocked, and the wind speed in the downtown area decreases, so the heat from air flow is less. Therefore, L1\2 the temperature in the city center will not rise, $T(L1)_{Case3} \approx T(L2)_{Case3}$ (as shown in the blue circle 1,1'). For the suburban section of A2 on axis L1, the temperature of Case2 and Case3 is significantly higher than that of Case1 due to the artificialization of the underlying surface (see the blue circle 2 in Fig. 11). However, the suburban section of B2 on axis L2 in Case2 locates at the downwind of the ventilation corridor, so the wind speed is large and thus the temperature is lower (see the blue circle 2' in Fig. 11). Generally speaking, the temperatures on the two axes can be ranked as $T_{Case3} > T_{Case2} \approx T_{Case1}$.

At 24:00, the heat generated in the expansion area of urban construction land flows gradually to the inner city along with the air flow. The temperature of each case from the central zone to the edge zone on the axes L1 and L2 still shows a trend from high to low. From the wind field Fig. 8(4), we can see that the wind direction of Case3 is basically parallel to the L1 axis, and the wind speed is the largest. Therefore, more heat is brought into the main urban area than other cases, and the temperature value of Case3 on axis L1 is highest. However in Case2, the warm and moist air blows to the L2 axis at this moment (see Figs. 7(4) and 8(4)), so the temperature value of

Case2 on axis L2 $T(L2)_{Case2}$ is the highest (see the L2 blue circle in Fig. 12). From the figure, we can see that the temperature on the two axes of Case1 at 24:00 is significantly lower than that of the other two cases. This indicates that the expansion of urban construction land will significantly increase the air temperature in the urban center at this moment.

5.5 Impacts of urban fringe construction land expansion on urban core area

To study the impact of urban construction land expansion on thermal environment in urban core areas, the temperature and heat island intensity index of the “Zhong Nan” with the highest urban land intensity (“H”) was extracted. The overall trend of temperature curve in Fig. 13(1) is basically consistent with that in Fig. 9. The temperature reaches minimum (25 °C) at 5:00. The temperatures in three cases reach maximum (over 35.5 °C) at 15:00, which is higher than the regional mean maximum temperature by 1 °C. From 0:00 to 20:00, the difference in temperature curve of three cases is small, while at 21:00, the difference occurs. This indicates that the expansion of urban construction land has little influence on the temperature of the urban core area. This phenomenon is early advanced by 8–9 h in Fig. 9. At 22:00, $T_{Case2} = T_{Case3}$, $T_{Case3} >$

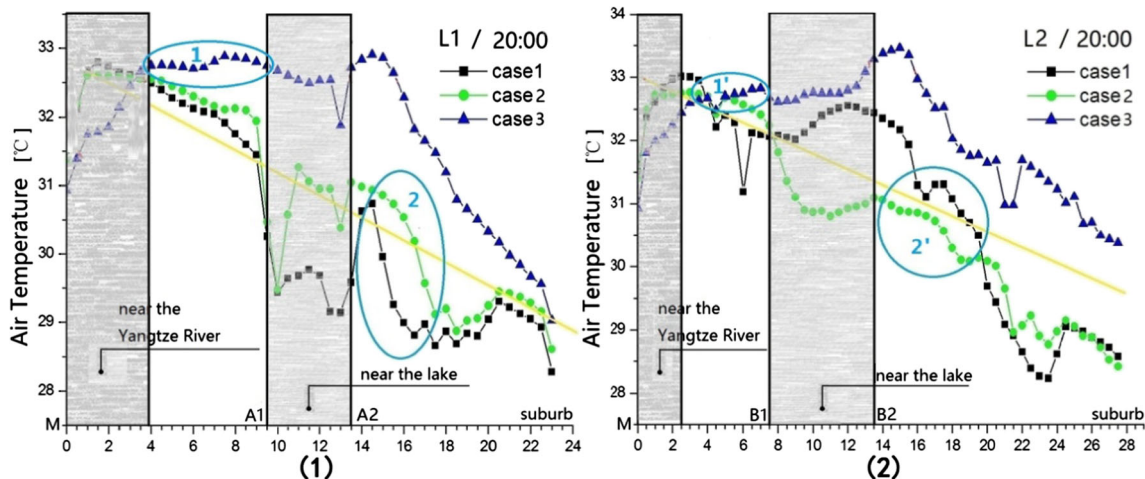


Fig. 11 Temperatures on L1/L2 at 20:00

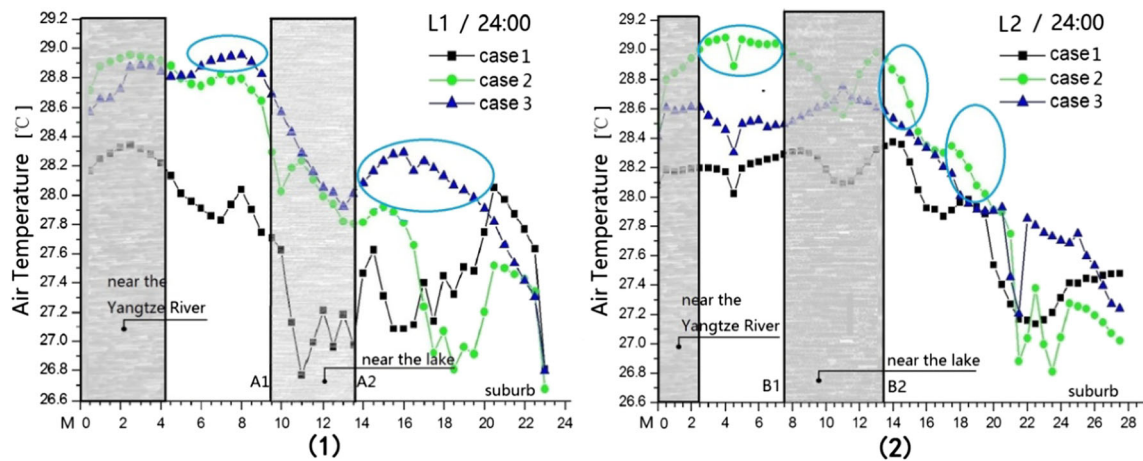


Fig. 12 Temperatures on L1/L2 at 24:00

$T_{\text{case1}} \approx 1.0^\circ\text{C}$. Within the next 1 h, T_{Case2} remains to be 29°C , while T_{Case3} starts to decrease sharply. At 23:00, there is $T_{\text{Case3}} = T_{\text{case1}} \approx 28.0^\circ\text{C}$, $T_{\text{Case2}} - T_{\text{case1}} > 1^\circ\text{C}$. This is because heat is constantly released from the water retained ventilation corridor in Case2, and transferred from the corridor to point “H.”

Figure 13(2) shows the heat island intensity curve at point “H,” and the three cases share the same reference point on the outskirts. For the three cases, the heat island intensity during 18:00–20:00 h is all greater than 2.5°C . From 8:00 to 14:00, due to the shading effect of high-intensity area inside the urban canopy, the temperature at point “H” is lower than that in the suburbs, and the urban heat island intensity has negative values. At 21:00, the difference in heat island intensity among three cases becomes significant. At 22:00, $T_{\text{Case2}} = T_{\text{Case3}}$, but heat island intensity in Case2 is slightly higher, indicating that the temperature at suburban reference point in Case2 is cooler than that in Case3 during this time period. From 23:00 to 24:00, Case1 and Case3 share coincident temperature curves and coincident heat island intensity curves. However, the

temperature in Case2 remains unchanged; the heat island strength increases significantly, which shows that the temperature at the reference point in the suburbs decreases significantly for such case. Therefore, we can conclude that the heat island intensity at core area “H” in Case2 is directly related to the effect of ventilation corridor during 22:00–24:00.

6 Conclusions

Wang and Li (2013) evaluated the spread level of 70 large and medium cities by using single index method, and pointed out that most cities in China (central and western) are in a low-density expansion. Therefore, blind urban sprawl and expansion is an urgent problem to be concerned with at present. It is the research direction of urban planning to rationally choose the expansion orientation of urban construction land and urban spatial evolution mode, and to study the change of urban underlying surface property in a multi-disciplinary way. After a series of data analysis, conclusions are drawn as follows:

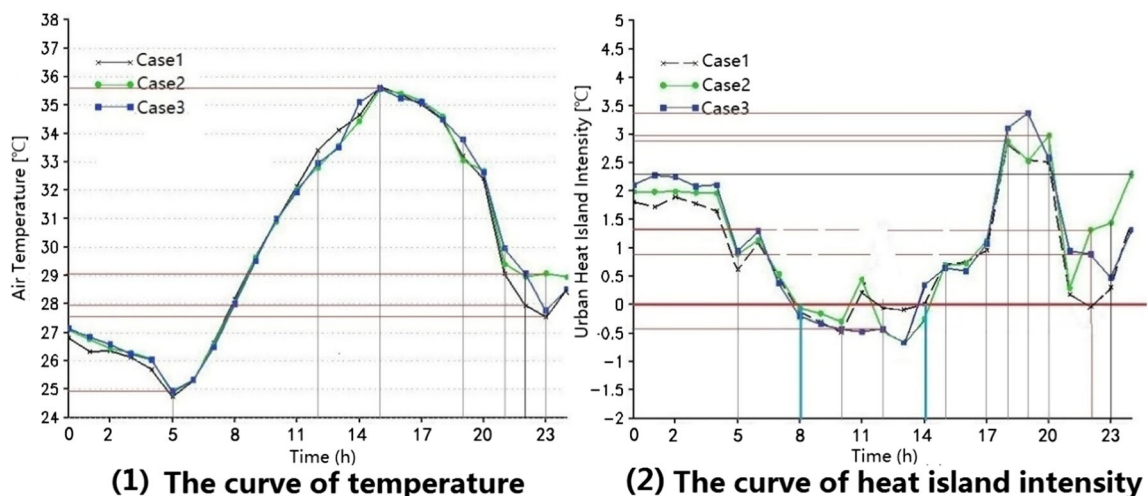


Fig. 13 Full-day temperature curve and heat island intensity curve at business circle “H”

- (1) From 5:00 to 12:00, the change of surface property has a very weak effect on urban temperature. From 12:00 to 5:00 of the next day, the situation varies from case to case, the expansion of construction land directly leads to the increase of temperature in the main urban area, the wider the expansion of construction land is, the greater the increase of temperature is. The high temperatures throughout the day range from 15:00–17:00.
- (2) The extension of urban construction land to the upper wind will generally increase the temperature of the whole city in summer. The change in the wind direction caused by the change of surface properties is more significant than the change in wind speed.
- (3) A ventilation corridor consisting of five lakes from south to north at the east bank of the Yangtze River is formed, which has the same wind direction as prevailing urban wind direction and is beneficial to heat diffusion in urban canopy. However, the slow heat dissipation of water in the corridor also affects the urban thermal environment at night.
- (4) During the period of intense sunshine at daytime, the interior of urban canopy, especially the area with high intensity of construction land, will produce cold island phenomenon due to the building sunshade.

Funding information This paper was supported by projects of the Hubei Province Natural Science Foundation of China (Project No. 2014CFB59), and the National Natural Science Foundation of China: Project No. 51538004.

References

- Chen F, Dudhia J (2001) Coupling an advanced land surface-hydrology model with the Penn State-NCAR MM5 Modeling System I. Part I: model implementation and sensitivity. *Mon Weather Rev* 129:569–585. [https://doi.org/10.1175/1520-0493\(2001\)129<0569:CAALSH>2.0.CO;2](https://doi.org/10.1175/1520-0493(2001)129<0569:CAALSH>2.0.CO;2)
- Chen Q, Srebric J (2000) Application of CFD tools for indoor and outdoor environment design. *Int J Archit Sci* 1:14–19 <https://www.ixueshu.com/document/303cfff1d30f6493318947a18e7f9386.html>
- Chen H, Ooka R, Huang H et al (2009) Study on mitigation measures for outdoor thermal environment on present urban blocks in Tokyo using coupled simulation. *Build Environ* 44(11):2290–2299. <https://doi.org/10.1016/j.buildenv.2009.03.012>
- Cleugh HA, Oke TR (1986) Suburban-rural energy balance comparisons in summer for Vancouver, B.C. *Bound-Layer Meteorol* 36:351–369 <https://link.springer.com/article/10.1007%2Fbfb00118337>
- Dong W, Cao Z (2016) Types of urbanization and urban development strategies. *Journal of Northeast University (Social Sciences)* 18: 137–142 (in Chinese). <https://doi.org/10.15936/j.cnki.1008-3758.2016.02.005>
- Dudhia J (1993) A nonhydrostatic version of the Penn State/NCAR mesoscale model: validation tests and simulation of an Atlantic cyclone and cold front. *Mon Weather Rev* 121(5):1493–1513. [https://doi.org/10.1175/1520-0493\(1993\)121<1493:ANVOTP>2.0.CO;2](https://doi.org/10.1175/1520-0493(1993)121<1493:ANVOTP>2.0.CO;2)
- Ek MB, Mitchell KE, Lin Y, Rogers E, Grunmann P, Koren V, Gayno G, Tarpley JD (2003) Implementation of Noah land surface model advances in the National Centers for Environmental Prediction operational mesoscale Eta model. *J Geophys Res* 108(D22):8851. <https://doi.org/10.1029/2002JD003296>
- Emmanuel R (2005) An urban approach to climate-sensitive design: strategies for the tropics. Spon Press, London and New York. <https://doi.org/10.4324/9780203414644>
- Gao S, Wanlong C, Zhu C, Zhu R et al (2001) Applied climatology. China Meteorological Press, Beijing (in Chinese)
- Gu C (2009) Climate changes and low-carbon city planning. Southeast University Press, Nanjing (in Chinese) <http://www.bookresource.net/pdf-7/txt-83798.html>
- Halstead MH (1979) Advances in software science. *Adv Comput* 18: 119–172. <https://doi.org/10.1023/A:1019207923078>
- Keyser D, Anthes RA (1997) The applicability of a mixed-layer model of the planetary boundary layer to real-data forecasting. *Mon Weather Rev* 105:1351–1371. [https://doi.org/10.1175/1520-0493\(1977\)105<1351:TAOAMM>2.0.CO;2](https://doi.org/10.1175/1520-0493(1977)105<1351:TAOAMM>2.0.CO;2)
- Kusaka H, Kondo H, Kikegawa Y, Kimura F (2001) A simple single-layer urban canopy model for atmospheric models: comparison with multi-layer and slab models. *Bound-Layer Meteorol* 101(3):329–358. <https://doi.org/10.1023/A:1019207923078>
- Li X, Chen H (2012) Observing the urban heat island in summer from city center to fringe—taking Wuhan as an example. *Green Ubiquitous Technol* 61(8):33–36. <https://doi.org/10.1109/GUT.2012.6344182>
- Li X, Chen H, Zhang S (2014) Quantitative study on the thermal environment of city spatial expansion—taking the southeast district of Wuhan as an example. *Urban Plann Forum* 3:71–76 (in Chinese) <http://www.docin.com/p-1369648340.html>
- Mellor GL, Yamada T (1982) Development of a turbulence closure model for geophysical fluid problems. *Rev Geophys* 20(4):851–875. <https://doi.org/10.1029/RG020i004p00851>
- Mielikainen J, Huang B, Huang HA, Goldberg MD (2012) GPU acceleration of the updated Goddard shortwave radiation scheme in the weather research and forecasting (WRF) model. *Appl Earth Observe Remote Sens* 5(2):555–562. <https://doi.org/10.1109/JSTARS.2012.2186119>
- Mlawer EJ, Taubman SJ, Brown PD, Iacono MJ, Clough SA (1997) Radiative transfer for inhomogeneous atmospheres: RRTM, a validated correlated-k model for the longwave. *J Geophys Res* 102(D14):16663–16682. <https://doi.org/10.1029/97JD00237>
- Monin AS, Obukhov AM (1954) Basic laws of turbulent mixing in the surface layer of the atmosphere. *Tr Akad Nauk SSSR Geophys. Inst* 24(151):163–187 <http://www.docin.com/p-232700734.html>
- National Center of Atmospheric Research (2012) ARW version 3 modeling system user's guide http://www2.mmm.ucar.edu/wrf/users/docs/user_guide_V4/WRFUsersGuide.pdf
- Pan X, Li X (2012) Research on the influence of the change of underlying surface on climate accuracy in Heihe river basin area by WRF. *Plateau Meteorol* 3:657–667 (in Chinese) <http://www.cnki.com.cn/Article/CJFDTotal-GYQX201203008.htm>
- Rao PK (1972) Remote sensing of urban heat islands from an environmental satellite. *Bull Am Meteorol Soc* 1972(53):647–648
- Statistical Bureau of Wuhan (2001) Wuhan 2001 statistical yearbook. China Publishing House, Beijing (in Chinese) <http://www.yearbookchina.com/navibooklist-N2008040026-1.html>
- Statistical Bureau of Wuhan (2011) Wuhan 2011 statistical yearbook. China Publishing House, Beijing (in Chinese) <http://www.whjt.gov.cn/tjnj/tjnj2011.pdf>
- The state council of the people's republic of china (2010) The State Council approved the Wuhan city general planning (in Chinese) <http://wenku.baidu.com/view/ab6edd6faf1ffc4ffe47ac5e.html>
- Thompson G, Rasmussen RM, Manning K (2004) Explicit forecasts of winter precipitation using an improved bulk microphysics scheme. Part I: description and sensitivity analysis. *Mon Weather* 132:519–542. [https://doi.org/10.1175/1520-0493\(2004\)132<0519:EFOWPU>2.0.CO;2](https://doi.org/10.1175/1520-0493(2004)132<0519:EFOWPU>2.0.CO;2)

- Wang J, Li Z (2013) Assessment of the spread level in Chinese big and medium cities. *J Zhongnan Univ Econ Law* 199(4):43–48 (in Chinese) <http://www.doc88.com/p-5337160355628.html>
- Wuhan people's government (2010) *2010–2020 Overall Urban Planning Overview in Wuhan* by People's Republic of China of Wuhan (in Chinese). <http://www.wpl.gov.cn/pc-35849-69-0.html>
- Xu Zhendong (2003) Research and analysis on the causes of urban heat island effect, Master's Thesis of Dalian University of Technology: 40–54 (in Chinese) <https://doi.org/10.7666/d.y635960>
- Yangtze River Daily (2009) Wuhan became the first pilot city of comprehensive transportation hub, Yangzi River Daily, 2009-08-28 (in Chinese) <http://www.mofcom.gov.cn/aarticle/resume/n/200908/20090806484772.html>
- Zhang G (2004) Progress and application prospect of WRF mode. *Meteorology* 30:27 (in Chinese). <https://doi.org/10.3969/j.issn.1000-0526.2004.12.006>
- Zhou X, Ooka R, Chen H (2014) Impacts of inland water area changes on the local climate of Wuhan, China. *Indoor Built Environ*. <https://doi.org/10.1177/1420326X14546774>